arxiv:1809.00962

BLIND PTYCHOGRAPHY BY DOUGLAS-RACHFORD SPLITTING

ALBERT FANNJIANG AND ZHEQING ZHANG

Abstract. Blind ptychography is the scanning version of coherent diffractive imaging which seeks to recover both the object and the probe simultaneously.

Based on alternating minimization by Douglas-Rachford splitting, AMDRS is a blind ptychographic algorithm informed by the uniqueness theory, the Poisson noise model and the stability analysis. Enhanced by the initialization method and the use of a randomly phased mask, AMDRS converges globally and geometrically.

Three boundary conditions are considered in the simulations: periodic, dark-field and bright-field boundary conditions. The dark-field boundary condition is suited for isolated objects while the bright-field boundary condition is for non-isolated objects. The periodic boundary condition is a mathematically convenient reference point. Depending on the availability of the boundary prior the dark-field and the bright-field boundary conditions may or may not be enforced in the reconstruction. Not surprisingly, enforcing the boundary condition improves the rate of convergence, sometimes in a significant way. Enforcing the bright-field condition in the reconstruction can also remove the linear phase ambiguity.

1. Introduction

Ptychography uses a localized coherent probe to illuminate different parts of a unknown extended object and collect multiple diffraction patterns as measurement data (Fig. 1). The redundant information in the overlap between adjacent illuminated spots is then exploited to improve phase retrieval methods [40, 43]. An important feature of ptychography [51, 52] is that the probe needs not be known precisely beforehand and can be recovered along with the unknown object.

Recently ptychography has been extended to the Fourier domain [41,61]. In Fourier ptychography, illumination angles are scanned sequentially with a programmable array source with the diffraction pattern measured at each angle [28, 54]. Tilted illumination samples different regions of Fourier space, as in synthetic-aperture and structured-illumination imaging.

Yet, despite significant progress that allows for reliable practical implementation, some of the technique's fundamentals remain poorly understood [48]. For example, precise conditions for uniqueness of blind-ptychographic solution are not known until recently. Roughly speaking the uniqueness theory [13] says that with the use of a randomly phased probe and for a general class of irregular scan schemes (e.g. (1) and (2)), called the mixing schemes, the only ambiguities are a scaling factor and an affine phase ramp, both of which are intrinsic to blind ptychographic reconstruction. In contrast, in standard, non-ptychographic phase retrieval the exit wave (the multiplication of the probe and the object) alone suffers ambiguities such as a global phase factor, a global spatial translation and the twin image. Further the exit wave in standard phase retrieval can not be unambiguously splitted into the probe and

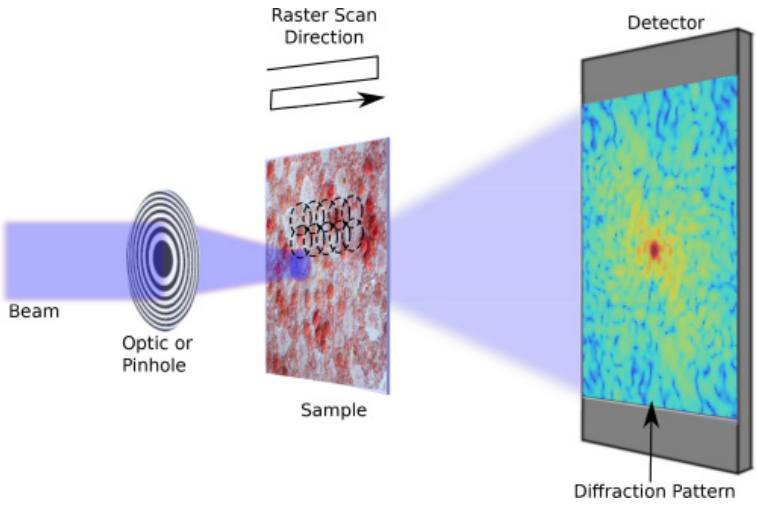

FIGURE 1. Simplified ptychographic setup showing a Cartesian grid used for the overlapping raster scan positions [37].

the object without other strong prior constraint [14]. This makes clear the fundamental advantage of the ptychographic method.

The purpose of this work is to present reconstruction schemes informed by the uniqueness theory, analyze the algorithmic structure and demonstrate by numerical experiments the global and geometrical convergence properties of the schemes.

We adopt the following notations in the paper. Let $\mathcal{T}$ be the set of all shifts, including $(0,0)$, involved in the ptychographic measurement. For general ptychographic schemes, we denote by $\mu^{\mathbf{t}}$ the $\mathbf{t}$-shifted probe for all $\mathbf{t} \in \mathcal{T}$ and $\mathcal{M}^{\mathbf{t}}$ the domain of $\mu^{\mathbf{t}}$. Let $f^{\mathbf{t}}$ the object restricted to $\mathcal{M}^{\mathbf{t}}$ and $\mathrm{Twin}(f^{\mathbf{t}})$ the twin image of $f^{\mathbf{t}}$ defined in $\mathcal{M}^{\mathbf{t}}$. We say that the object part $f^{\mathbf{t}}$ has a tight support in $\mathcal{M}^{\mathbf{t}}$ if $\mathcal{M}^{\mathbf{t}}$ does not fully contain any spatially shifted support of $f^{\mathbf{t}}$. Let $f := \cup_{\mathbf{t}} f^{\mathbf{t}} \subseteq \mathcal{M} := \cup_{\mathbf{t}} \mathcal{M}^{\mathbf{t}}$.

Several ideas can be drawn from the uniqueness theory [13] that prescribes precise conditions under which ptychographic ambiguities are limited to a scaling factor and an affine phase ramp.

First the theory recommends the use of irregular perturbations of raster scan of step size τ which have been widely practiced in the literature. One is

(1) Rank-one perturbation $\quad \mathbf{t}_{kl} = \tau(k,l) + (\delta_k^1, \delta_l^2), \quad k,l \in \mathbb{Z}$

where δ_k^1 and δ_l^2 are small random variables relative to τ. The other is

(2) Full-rank perturbation $\quad \mathbf{t}_{kl} = \tau(k,l) + (\delta_{kl}^1, \delta_{kl}^2), \quad k,l \in \mathbb{Z}$

where δ_{kl}^1 and δ_{kl}^2 are small random variables relative to τ.

Second the theory recommends the use of a randomly phased probe with the unknown transmission function $\mu^0(\mathbf{n}) = |\mu^0|(\mathbf{n})e^{\mathrm{i}\theta(\mathbf{n})}$ where $\theta(\mathbf{n})$ are random variables and $|\mu^0|(\mathbf{n}) \neq 0, \forall \mathbf{n} \in \mathcal{M}^0$. Randomly phased probes have been adopted in ptychographic experiments [33, 36, 42, 49].

Third, the theory suggests the probe phase constraint (PPC) as the probe initialization. *We say that a probe estimate ν^0 satisfies PPC with $\delta < 1$ if*

$$\measuredangle(\nu^0(\mathbf{n}), \mu^0(\mathbf{n})) < \delta\pi, \quad \forall \mathbf{n}. \tag{3}$$

The default case is $\delta = 1/2$ and PPC has the intuitive meaning $\Re(\bar{\nu}^0 \odot \mu^0) > 0$ at every pixel (where $\odot$ denotes the component-wise product, the bar the complex conjugate and $\Re$ the real part), which implies certain similarity of ν^0 to μ^0.

The constraint (3) represents prior information about the probe and, in practice, needs only to hold for sufficiently large number of pixels $\mathbf{n}$. We use (3) for selecting and quantifying initialization, instead of the usual 2-norm.

Fourth, the theory advises a probe size and overlap such that the objects parts $\{f^{\mathbf{t}} : \mathbf{t} \in \mathcal{T}\}$ mutually overlap sufficiently and at least one part $f^{\mathbf{t}}$ has a tight support in $\mathcal{M}^{\mathbf{t}}$. The reader is referred to [13] for the technical definition of sufficient overlap which depends not only on the overlap of adjacent illuminations but also on the object support. For example, the overlap requirement of adjacent illuminations for a sparsely supported object is higher than that for a densely support object. In the literature, the adjacent illuminations have at least 50%, typically 60-70%, overlap [3, 34]. This rule of thumb is more stringent than necessary in the case of an extended, densely supported object.

1.1. **Our contribution.** Our reconstruction scheme is based on alternating minimization with the Douglas-Rachford splitting (DRS) method. DRS is a proximal point method closely related to the Alternating Direction Method of Multipliers (ADMM). The existing theory and analysis for DRS and ADMM (see, e.g. [12,17,19,30]) are limited to the convex optimization, except for a few exceptions (see e.g. [5, 22, 29]). In particular, the performance of DRS and ADMM in the non-convex setting depends sensitively on the choice of the objective functions as well as the selection of the relaxation parameters and the step size which are the main focus of our proposed scheme.

Our choices of the objective functions and the step size are informed by the uniqueness theory [13], the Poisson noise model and the stability analysis. The confluence of the three considerations leads to the proposed scheme (acronym AMDRS). The crux of our stability analysis (Proposition 2.1 and 2.2) is that the true solution (modulo the scaling factor and the affine phase ambiguity) to blind ptychography is stable fixed point of AMDRS with any step size and, moreover, in the case of the unit step size, all other fixed points are saddle points. This suggests that a unit step size is a good choice for AMDRS in contrast to (sufficiently) small step sizes typically required for nonconvex convergence analysis [22, 29].

For any iterative scheme for non-convex optimization, the initialization of the iteration plays a crucial role in the convergence of the scheme. The initialization step is often glossed over in the development of numerical schemes due to lack of a good metric (see e.g. [32, 51, 57]). In our numerical experiments, PPC turns out to be an excellent initialization method and metric for controlling the convergence behavior of the schemes. In particular, our schemes converge globally and geometrically under PPC with $\delta = 1/2$.

In additional to demonstrate the numerical performance of the proposed schemes, we propose a special boundary condition (the bright-field boundary condition) to remove the linear phase

ambiguity. The capability of removing the linear phase ambiguity is particularly important for 3D blind tomography as the different linear phase ramps for different projections would collectively create enormous 3D ambiguities that are difficult to make consistent.

The rest of the paper is organized as follows. In Section 2, we introduce the Douglas-Rachford splitting method as the key ingredient of our reconstruction algorithms, Gaussian-DRS and Poisson-DRS. We give the fixed point analysis in Section 2.3. In Section 3, we perform numerical experiments with our schemes. In Appendix A, we show that Gaussian-DRS is an asymptotic form of Poisson-DRS. We conclude in Section 4.

2. Alternating minimization by Douglas-Rachford splitting

For simplicity, let $\mathrm{supp}(f) \subseteq \mathbb{Z}_n^2 \subseteq \mathcal{M}$ and let $\mathcal{M}^0 := \mathbb{Z}_m^2, m < n$, be the initial probe region with the structured illumination given by μ^0. The pixels in $\mathcal{M} \setminus \mathbb{Z}_n^2$ merits a separate treatment (referred to as boundary condition) depending on the experimental set-up (see Section 3.7).

Let $\mathcal{F}(\nu, g) \in \mathbb{C}^N$ be the totality of the Fourier (magnitude and phase) data corresponding to the probe ν and the object g such that $|\mathcal{F}(\mu, f)| = b$ where b is the noiseless ptychographic data. Since $\mathcal{F}(\cdot, \cdot)$ is a bilinear function, $A_k h := \mathcal{F}(\mu_k, h),\ k \geq 1$, defines a matrix A_k for the k-th probe estimate μ_k and $B_k \eta := \mathcal{F}(\eta, f_{k+1}),\ k \geq 1$, for the $(k+1)$-st image estimate f_{k+1} such that $A_k f_{j+1} = B_j \mu_k,\ j \geq 1, k \geq 1$.

For any $y \in \mathbb{C}^{m \times m}$, $\mathrm{sgn}(y)$ is defined as

$$\mathrm{sgn}(y)[j] = \begin{cases} 1 & \text{if } y[j] = 0 \\ y[j]/|y[j]| & \text{else.} \end{cases}$$

The basic strategy for blind ptychographic reconstruction is to alternately update the object and probe estimates starting from an initial guess [14, 51, 52]. We pursue the same strategy and perform the object and probe updates by solving certain minimization problems.

Algorithm 1: Alternating minimization (AM)

1: Input: initial probe guess $\mu_1 \in \mathrm{PPC}(\mathbf{k}, \delta)$.
2: Update the object estimate $\quad f_{k+1} = \arg\min \mathcal{L}(A_k g)$ s.t. $g \in \mathbb{C}^{n \times n}$.
3: Update the probe estimate $\quad \mu_{k+1} = \arg\min \mathcal{L}(B_k \nu)$ s.t. $\nu \in \mathbb{C}^{m \times m}$.
4: Terminate if $\||B_k \mu_{k+1}| - b\|_2$ stagnates or is less than tolerance; otherwise, go back to step 2 with $k \to k+1$.

2.1. Alternating minimization.

A main feature of alternating minimization scheme is the monotonicity property:

$$\mathcal{L}(A_k f_k) \geq \mathcal{L}(A_{k+1} f_{k+1}), \quad \mathcal{L}(B_k \mu_k) \geq \mathcal{L}(B_{k+1} \mu_{k+1}).$$

We consider two log-likelihood cost functions [2, 53] for noise-robustness

$$\text{Poisson:}\quad \mathcal{L}(y) = \sum_i |y[i]|^2 - b^2[i] \ln |y[i]|^2 \tag{4}$$

$$\text{Gaussian:}\quad \mathcal{L}(y) = \frac{1}{2}\||y| - b\|_2^2 \tag{5}$$

based on the maximum likelihood principle for the Poisson noise model. The Poisson log-likelihood function (4) is asymptotically reduced to (5) as shown in Appendix A.

The ptychographic iterative engines, PIE [45], ePIE [34] and rPIE [32], are both derived from the amplitude-based cost function (5). The maximum likelihood scheme is also a variance stabilization scheme which uniformizes the probability distribution for every pixel regardless of the measured intensity value [27]. It is well established that the amplitude-based cost function (5) outperforms the intensity-based cost function $\frac{1}{2}\||y|^2 - b^2\|_2^2$ [57]. See [20, 60] for more choices of objective functions.

For non-convex iterative optimization, a good initial guess or some regularization is usually crucial for convergence [2, 53]. Here we consider a rough initialization for the probe. To test the linear phase ambiguity, we also consider the probe initialization

$$\mu_1(\mathbf{n}) = \mu^0(\mathbf{n}) \exp\left[\mathrm{i}2\pi \frac{\mathbf{k}\cdot\mathbf{n}}{n}\right] \exp\left[\mathrm{i}\phi(\mathbf{n})\right], \quad \mathbf{n} \in \mathcal{M}^0 \tag{6}$$

where $\phi(\mathbf{n})$ are independently and uniformly distributed on $(-\delta\pi, \delta\pi)$. We use $\delta \in [0, 1/2]$ as the control parameter for the proximity of the initial probe to the true probe, modulo a linear phase factor represented by $\mathbf{k}$, and denote this class of probe initialization by $\mathrm{PPC}(\mathbf{k}, \delta)$.

2.2. **DR splitting (DRS).** We formulate the inner loops (Step 2 and 3 in Algorithm 1) of AM as

$$\min_u K(u) + \mathcal{L}(u) \tag{7}$$

where the additional objective function K enforces the constraint that u is in the range of A_k or B_k.

We solve (7) by the Douglas-Rachford splitting (DRS) method which is a proximal point algorithm for minimizing a sum of two objective functions [12, 30]. This is motivated by the good performance of the classical Douglas-Rachford (CDR) algorithm [10, 30] (aka the difference map [11] in the optics literature), a special case of DRS with an infinitely large step size, which has been used for ptychographic reconstruction [51, 52, 56] and analyzed in [5, 6]. The CDR iteration, however, exhibits only a sub-linear convergence globally in the noiseless case [5] and, when the optimization problems become infeasible (e.g. with noisy data), tends to fluctuate and underperform, hence the search for a faster convergent and more robust DRS.

DRS is defined by the following iteration for $l = 1, 2, 3 \cdots$

$$
\begin{aligned}
y^{l+1} &= \mathrm{prox}_{K/\rho}(u^l); \\
z^{l+1} &= \mathrm{prox}_{\mathcal{L}/\rho}(2y^{l+1} - u^l) \\
u^{l+1} &= u^l + z^{l+1} - y^{l+1}
\end{aligned} \tag{8}
$$

where $\mathrm{prox}_{\mathcal{L}/\rho}(u^k) := \underset{x}{\mathrm{argmin}}\, \mathcal{L}(x) + \frac{\rho}{2}\|x - u^k\|^2$. For the initial guess u_1^1 in our simulations, we let $u_1^1 = A_1^* f_1$ where $f_1(\mathbf{n})$ is a phase object with i.i.d. phase uniformly distributed over $[0, 2\pi]$ or a constant value 0. Here $\gamma = 1/\rho$ is often referred to as the step size of DRS.

It can be checked that DRS (7) is formally equivalent to the Alternating Direction Method of Multipliers (ADMM)

$$\max_{\lambda} \min_{y,z} \mathcal{L}(y) + K(z) + \langle \lambda, y - z \rangle + \frac{\rho}{2}\|z - y\|^2.$$

Our choice of K is important to our implementation of DRS. Since the object estimate in the $k-$th epoch must be of the form $A_k g$ for some $g \in \mathbb{C}^{n \times n}$, we let $K(u)$ be the indicator function $\chi_k(u)$ of the range of A_k, i.e. $\chi_k(u) = 0$ if y is in the range of A_k^*; and $\chi_k(u) = \infty$ otherwise. For this choice of K, $\mathrm{prox}_{K/\rho}(u) = P_k u$ is independent of ρ. This should be contrasted with the choice of the distance function adopted in [29] for the tractability of the convergence analysis due to the smoothness of the distance function.

For the Gaussian case (5), we update the object estimate as

$$f_{k+1} = A_k^\dagger u_k^\infty \tag{9}$$

where u_k^∞ is the terminal output of the following iteration

$$y_k^l = A_k A_k^\dagger u_k^l \tag{10}$$

$$z_k^l = \frac{1}{\rho + 1} b \odot \mathrm{sgn}(2y_k^l - u_k^l) + \frac{\rho}{\rho + 1}(2y_k^l - u_k^l) \tag{11}$$

$$u_k^{l+1} = u_k^l + z_k^l - y_k^l. \tag{12}$$

Substituting (10) and (11) into (12) and reorganizing the resulting equation, we obtain

$$
\begin{aligned}
u_k^{l+1} &= \frac{1}{\rho + 1} u_k^l + \frac{\rho - 1}{\rho + 1} P_k u_k^l + \frac{1}{\rho + 1} b \odot \mathrm{sgn}\big(2P_k u_k^l - u_k^l\big) \\
&= \frac{1}{2} u_k^l + \frac{\rho - 1}{2(\rho + 1)} R_k u_k^l + \frac{1}{\rho + 1} b \odot \mathrm{sgn}\big(R_k u_k^l\big)
\end{aligned} \tag{13}
$$

where $P_k = A_k A_k^\dagger$ is the orthogonal projection onto the range of A_k and $R_k = 2P_k - I$ is the corresponding reflector. We set $u_k^1 = u_{k-1}^\infty$ where u_{k-1}^∞ is the terminal value at epoch $k - 1$.

Likewise, we update the probe as

$$\mu_{k+1} = B_k^\dagger v_k^\infty \tag{14}$$

where v_k^∞ is the terminal output of the following iteration

$$
\begin{aligned}
v_k^{l+1} &= \frac{1}{\rho+1}v_k^l + \frac{\rho-1}{\rho+1}Q_k v_k^l + \frac{1}{\rho+1}b\odot \operatorname{sgn}\Big(2Q_k v_k^l - v_k^l\Big) \\
&= \frac{1}{2}v_k^l + \frac{\rho-1}{2(\rho+1)}S_k u_k^l + \frac{1}{\rho+1}b\odot \operatorname{sgn}\big(S_k v_k^l\big)
\end{aligned} \tag{15}
$$

where $Q_k = B_k B_k^\dagger$ is the orthogonal projection onto the range of B_k and S_k the corresponding reflector. We set $v_k^1 = v_{k-1}^\infty$ where v_{k-1}^∞ is the terminal value at epoch $k-1$.

For the Poisson case (4), the inner loops take a more complicated form

$$
u_k^{l+1} = \frac{1}{2}u_k^l - \frac{1}{\rho+2}R_k u_k^l + \frac{\rho}{2\rho+4}\sqrt{|R_k u_k^l|^2 + \frac{8(2+\rho)}{\rho^2}b^2}\odot \operatorname{sgn}\Big(R_k u_k^l\Big) \tag{16}
$$

$$
v_k^{l+1} = \frac{1}{2}v_k^l - \frac{1}{\rho+2}S_k v_k^l + \frac{\rho}{2\rho+4}\sqrt{|S_k v_k^l|^2 + \frac{8(2+\rho)}{\rho^2}b^2}\odot \operatorname{sgn}\Big(S_k v_k^l\Big) \tag{17}
$$

After the inner loops terminate, we update the object and probe as (9) and (14),respectively.

We shall refer to DRS with the Poisson log-likelihood function (16)-(17) and the Gaussian version (13)-(15) by the acronyms *Poisson-DRS* and *Gaussian-DRS*, respectively. We call the the two algorithms the Alternating Minimization with Douglas-Rachford Splitting (AM-DRS). Due to the non-differentiability of both K and $\mathcal{L}$, the global convergence property of the proposed DRS method is beyond the current framework of analysis [29].

In the limiting case of $\rho \to 0$, both Gaussian-DRS and Poisson-DRS become the classical Douglas-Rachford algorithm.

The computation involved in Gaussian-DRS and Poisson-DRS are mostly pixel-wise operations (hence efficient) except for the pseudoinverses $A_k^\dagger = (A_k^* A_k)^{-1}A_k^*$ and $B_k^\dagger = (B_k^* B_k)^{-1}B_k^*$. In blind ptychography, due to the isometry of the Fourier transform, $A_k^* A_k$ and $B_k^* B_k^\dagger$ are diagonal matrices and easy to invert [13].

2.3. **Fixed points of Gaussian-DRS.** For simplicity, we shall focus the stability analysis on the fixed points of Gaussian DRS.

Suppose that the limit $(u, v) = \lim_{k,l\to\infty}(u_k^l, v_k^l)$ exist where (u_k^l, v_k^l) are two-parameter arrays of the Gaussian-DRS iterates. Let $\lim_{k\to\infty} A_k = A_\infty,\ \lim_{k\to\infty} B_k = B_\infty$.

Let $P_\infty = A_\infty A_\infty^\dagger$ and $Q_\infty = B_\infty B_\infty^\dagger$ denote the orthogonal projection onto the range of A_∞ and B_∞, respectively. Let $P_\infty^\perp = I - P_\infty$ and $Q_\infty^\perp = I - Q_\infty$ denote the orthogonal complements of P_∞ and Q_∞, respectively. Denote $R_\infty = 2P_\infty - I, S_\infty = 2Q_\infty - I$.

Passing to the limit in (13)-(15) we obtain the fixed point equation for Gaussian-DRS

$$
u = \frac{1}{2}u + \frac{\rho-1}{2(\rho+1)}R_\infty u + \frac{1}{\rho+1}b\odot \operatorname{sgn}\big(R_\infty u\big) \tag{18}
$$

$$
v = \frac{1}{2}v + \frac{\rho-1}{2(\rho+1)}S_\infty v + \frac{1}{\rho+1}b\odot \operatorname{sgn}\big(S_\infty v\big) \tag{19}
$$

It is straightforward to check that the true solution $(u_0 := \mathcal{F}(\mu, f), v_0 := \mathcal{F}(\mu, f))$ is a fixed point of Gaussian-DRS (13)-(15) and Poisson-DRS (16)-(17).

We now give theoretical motivation for our numerical choice of $\rho = 1$.

For a solution (u, v) to the fixed point equation (18)-(19), define the reflection images, $x := R_\infty u,\ y := S_\infty v$. Denote the right hand side of (18) as $U(x)$ and consider a perturbation of x by ϵz where ϵ is a small positive number. Set $\Omega = \mathrm{diag}(\mathrm{sgn}(x))$, $C = \Omega^* A_\infty$, $\eta = \Omega^* z$. Suppose $|x| > 0$. From somewhat tedious but straightforward calculation, we have

$$\lim_{\epsilon \to 0} \frac{1}{\epsilon}(U(x + \epsilon v) - U(x)) \quad = \quad \Omega J_A(\eta)$$

where

$$J_A(\eta) \quad = \quad CC^\dagger \eta - \frac{1}{1+\rho}\left[\Re\big(2CC^\dagger\eta - \eta\big) + \imath\big(I - \mathrm{diag}(b/|x|)\big)\Im\left(2CC^\dagger\eta - \eta\right)\right]. \tag{20}$$

The differential J_B of the right hand side of (19) has the similar structure.

We prove the following results in Appendix B and C. The first result says that for $\rho = 1$ all the non-solution fixed points are linearly unstable and the second says that for $\rho \in [0, \infty)$ the true solutions to blind ptychography are stable fixed points.

Proposition 2.1. *Let (u, v) be a solution to (18)-(19) with $\rho = 1$ such that $|x| > 0$ or $|y| > 0$. Suppose*

$$\|J_A(\eta)\|_2 \le \|\eta\|_2, \quad \forall \eta \in \mathbb{C}^N \quad \textit{or} \quad \|J_B(\xi)\|_2 \le \|\xi\|_2, \quad \forall \xi \in \mathbb{C}^N$$

where N is the dimension of data. Then $f_\infty := A_\infty^\dagger u$ and $\mu_\infty := B_\infty^\dagger v$ are a solution to blind ptychography, i.e. $|\mathcal{F}(\mu_\infty, f_\infty)| = b$. Moreover, we have

$$x = A_\infty f_\infty = b \odot \mathrm{sgn}(x) = B_\infty \mu_\infty = y. \tag{21}$$

Proposition 2.2. *Let (u, v) be a solution to (18)-(19) for any $\rho \in [0, \infty)$ such that*

$$|\mathcal{F}(\mu_\infty, f_\infty)| = b$$

where μ_∞ and f_∞ are defined as in Proposition 2.1. Then

$$\|J_A(\eta)\|_2 \le \|\eta\|_2, \quad \|J_B(\xi)\|_2 \le \|\xi\|_2$$

for all $\eta, \xi \in \mathbb{C}^N$ and the equality holds in the direction $\pm \imath b/\|b\|$ (and possibly elsewhere on the unit sphere).

Moreover, under the uniqueness conditions of [13], Proposition 2.1 and 2.2 then imply that the true solution and its inherent ambiguities (modulo a scaling factor and affine phase ramp) are the only stable fixed points of Gaussian-DRS with the unit step size. Therefore Gaussian-DRS with the unit step size should not stagnate near a fixed point that is not a solution to blind ptychography.

(a) (b)

FIGURE 2. (a) The real part and (b) the imaginary part of the first test image.

3. Experiments

As motivated by Proposition 2.1, we fix the DRS parameter $\rho = 1$ in all simulations. As a result, (13)-(15) become

$$\begin{aligned} u_k^{l+1} &= \frac{1}{2}u_k^l + \frac{1}{2}b \odot \mathrm{sgn}\big(R_k u_k^l\big) \\ v_k^{l+1} &= \frac{1}{2}v_k^l + \frac{1}{2}b \odot \mathrm{sgn}\Big(S_k v_k^l\Big). \end{aligned}$$

and (16)-(17) become

$$\begin{aligned} u_k^{l+1} &= \frac{1}{2}u_k^l - \frac{1}{3}R_k u_k^l + \frac{1}{6}\sqrt{|R_k u_k^l|^2 + 24b^2} \odot \mathrm{sgn}\Big(R_k u_k^l\Big) \\ v_k^{l+1} &= \frac{1}{2}v_k^l - \frac{1}{3}S_k v_k^l + \frac{1}{6}\sqrt{|S_k v_k^l|^2 + 24b^2} \odot \mathrm{sgn}\Big(S_k v_k^l\Big). \end{aligned}$$

3.1. **Test objects.** Our first test image is 256-by-256 Cameraman+ i Barbara (CiB). The resulting test object has the phase range $\pi/2$. The second test object is randomly-phased phantom (RPP) defined by $f_* = P \odot e^{\mathrm{i}\phi}$ where P is the standard phantom (Fig. 3(a)) and $\{\phi(\mathbf{n})\}$ are i.i.d. uniform random variables over $[0, 2\pi]$. RPP has the maximal phase range because of its noise-like phase profile. In addition to the huge phase range, RPP has loosely supported parts with respect to the measurement schemes (see below) due to its thick dark margins around the oval.

3.2. **Measurement schemes.** We do not explore the issue of varying the probe size in the present work, which has been done with the classical Douglas-Rachford algorithm in [6]. We fix the probe size to 60×60. In addition to the i.i.d. probe, we consider also correlated probe produced by convolving the i.i.d. probe with characteristic function of the

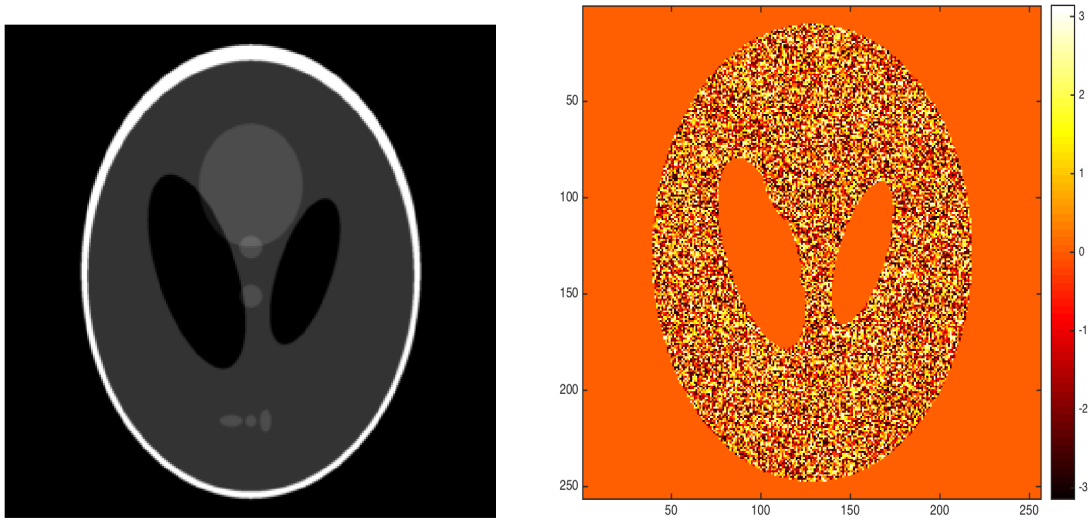

(a) RPP magnitudes (b) RPP phases

FIGURE 3. (a) Magnitudes and (b) phases of RPP.

set $\{(k_1, k_2) \in \mathbb{Z}^2 : \max\{|k_1|, |k_2|\} \leq c \cdot m;\ c \in (0, 1]\}$ where the constant c is a measure of the correlation length in the unit of $m = 60$ (Fig. 4).

We let δ_k^1 and δ_l^2 in the rank-one scheme (1) and δ_{kl}^1 and δ_{kl}^2 in the full-rank scheme (2) to be i.i.d. uniform random variables over $[\![-4, 4]\!]$. In other words, the adjacent probes overlap by an average of $\tau/m = 50\%$.

3.3. **Initialization.** As explained in Section 2.1, we use (6) to initialize the probe estimate in all experiements.

If the probe is exactly known (i.e. $\mathbf{k} = 0$, $\delta = 0$), there is a direct method to initialize the object estimate by feature extraction even in the case of the regular raster scan without perturbations (i.e. $\delta_{kl}^1 = \delta_{kl}^2 = 0$) as demonstrated in Appendix D.

3.4. **Error metrics.** We use relative error (RE) and relative residual (RR) as the merit metrics for the recovered image f_k and probe μ_k at the k^{th} epoch:

$$\text{RE}(k) = \min_{\alpha \in \mathbb{C}, \mathbf{k} \in \mathbb{R}^2} \frac{\|f(\mathbf{k}) - \alpha e^{-\imath 2\pi \mathbf{k} \cdot \mathbf{r}/n} f_k(\mathbf{k})\|_2}{\|f\|_2} \tag{22}$$

$$\text{RR}(k) = \frac{\|b - |A_k f_k|\|_2}{\|b\|_2}. \tag{23}$$

Note that in (22) the linear phase ambiguity is discounted along with a scaling factor.

3.5. **Different combinations.** First we compare performance of AMDRS with different combinations of objective functions, scanning schemes and random probes in the case of noiseless measurements with the periodic boundary condition. We use the stopping criteria

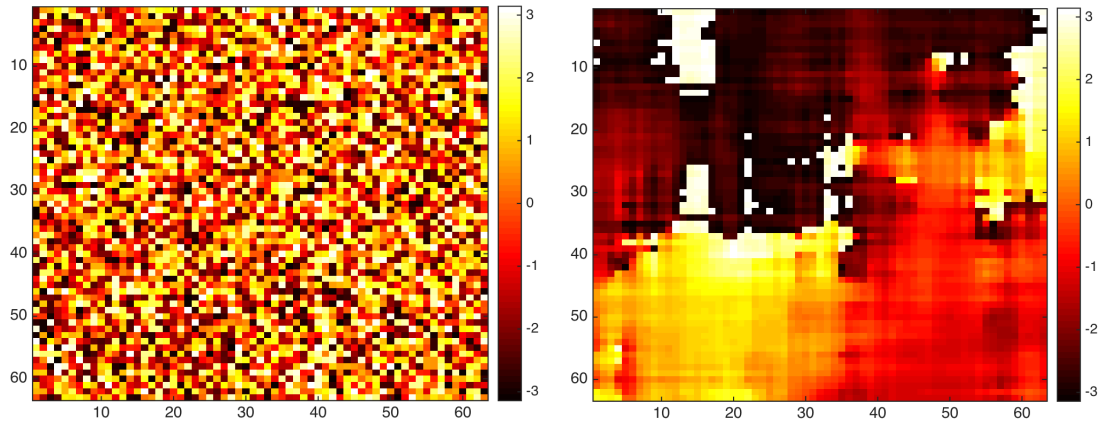

(a) i.i.d. probe (b) Correlated probe $c = 0.4$

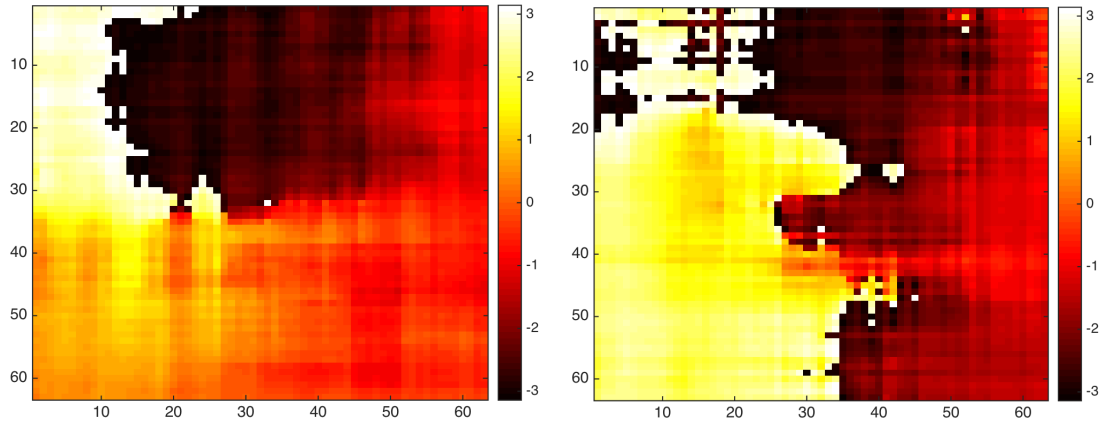

(c) Correlated probe $c = 0.7$ (d) Correlated probe $c = 1$

FIGURE 4. The phase profile of (a) the i.i.d. probe and (b)(c)(d) the correlated probes of various correlation lengths.

for the inner loops:

$$\frac{\||A_k A_k^\dagger u_k^l| - b\|_2 - \||A_k A_k^\dagger u_k^{l+1}| - b\|_2}{\||A_k A_k^\dagger u_k^l| - b\|_2} \leq 10^{-4}$$

with the maximum number of iterations capped at 60.

Figure 5 shows geometric decay of RE (22) at various rates r_o for the test object CiB. In particular, Fig. 5(a) shows that the full-rank scheme outperforms the rank-one scheme and that Poisson-DRS outperforms (slightly) Gaussian-DRS while Figure 5(b) shows that the i.i.d. probe yields the smallest rate of convergence ($r_o = 0.7562$) closely followed by the rate ($r_o = 0.7583$) for $c = 0.4$.

3.6. **Poisson noise.** For noisy measurement, the level of noise is measured in terms of the noise-to-signal ratio (NSR).

$$\text{NSR} = \frac{\|b - |A_0 f_0|\|_2}{\|A_0 f_0\|_2}$$

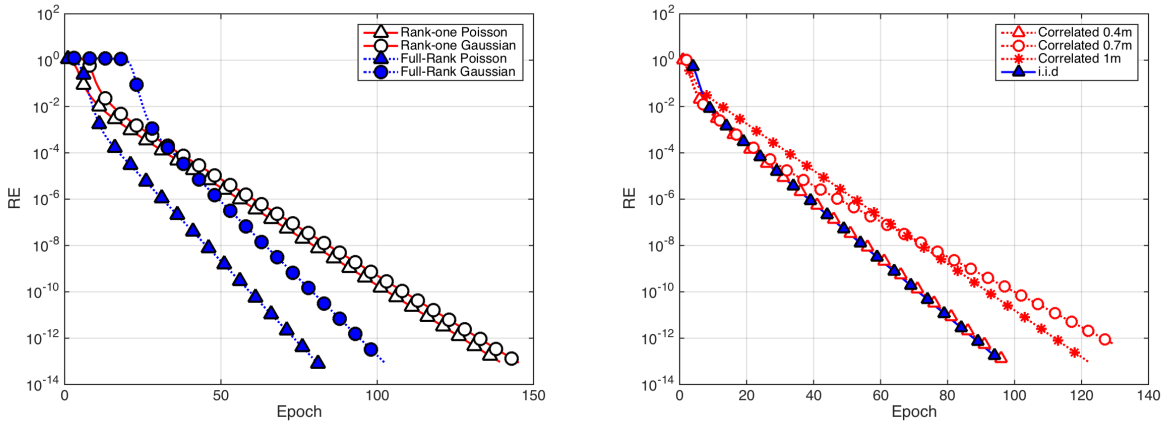

(a) (b)

FIGURE 5. Geometric convergence to CiB at various rates for (a) Four combinations of objective functions and scanning schemes with i.i.d. probe (rank-one Poisson, $r_o = 0.8236$; rank-one Gaussian, $r_o = 0.8258$; full-rank Poisson, $r_o = 0.7205$; full-rank Gaussian, $r_o = 0.7373$) and (b) Poisson-DRS with four probes of different correlation lengths ($r_o = 0.7583$ for $c = 0.4$; $r_o = 0.8394$ for $c = 0.7$; $r_o = 0.7932$ for $c = 1$; $r_o = 0.7562$ for iid probe)

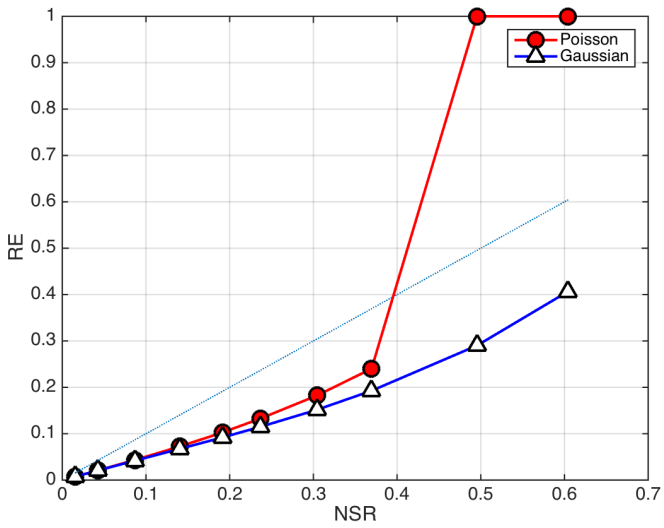

FIGURE 6. RE versus NSR

Figure 6 shows RE (22) for CiB versus NSR for Poisson-DRS and Gaussian-DRS with the periodic boundary condition, i.i.d. probe and the full-rank scheme. The maximum number of epoch in AMDRS is limited to 100. The RR stabilizes usually after 30 epochs. The (blue) reference straight line has slope 1. We see that the Gaussian-DRS outperforms the Poisson-DRS, especially when the Poisson RE becomes unstable for NSR $\geq 35\%$. As noted

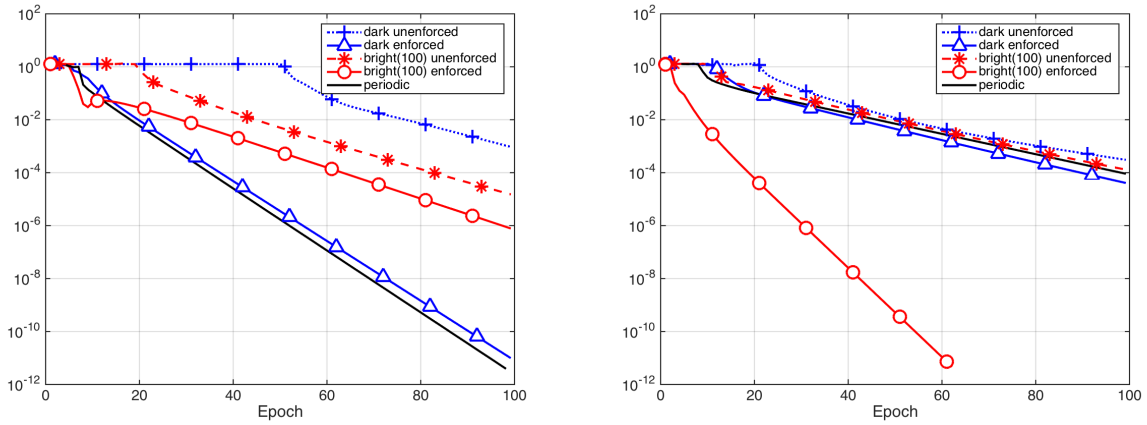

(a) CiB reconstruction with PPC(0, 0, 0.5)

(b) RPP reconstruction with PPC(0, 0, 0.4)

FIGURE 7. RE under various boundary conditions

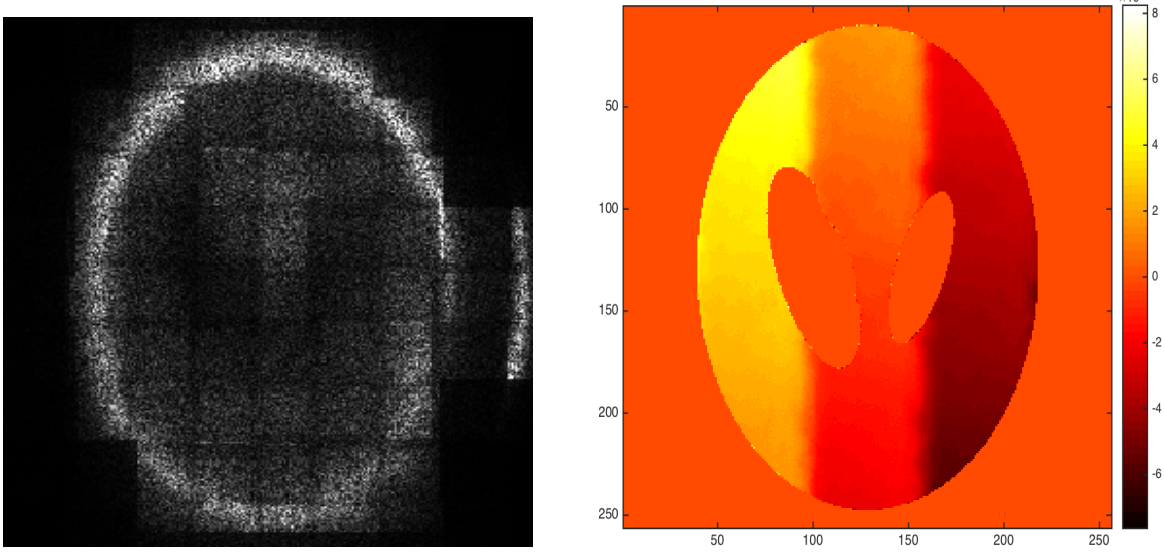

(a) Reconstructed moduli with dark BC & 30 inner iterations

(b) Reconstructed phase error with periodic BC & 80 inner iterations

FIGURE 8. RPP reconstruction with PPC(0, 0, 0.5) and (a) the dark-field BC & (b) the periodic BC.

in [8, 32, 62] fast convergence (with the Poisson log-likelihood function) may introduce noisy artifacts and reduce reconstruction quality.

For the rest of the experiments, we use noiseless data, Poisson-DRS and the full-rank scheme.

3.7. **Boundary conditions.** When the probe steps outside of the boundary of the object domain, the area $\mathcal{M} \setminus \mathbb{Z}_n^2$ needs special treatment in the reconstruction process.

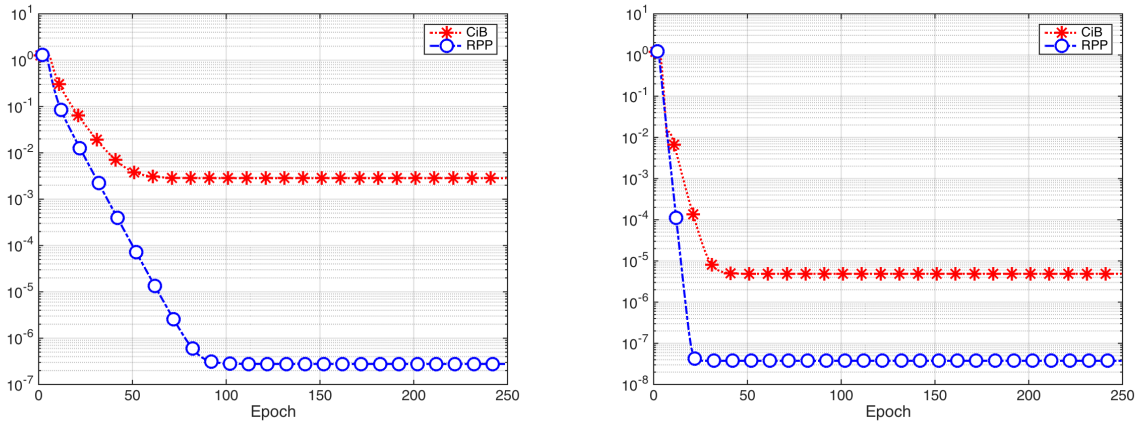

(a) Boundary value = 100 (b) Boundary value = 255

FIGURE 9. RE with PPC(-0.5, 0.5, $\frac{1}{2}$) and the boundary value (a) 100 and (b) 255

The periodic boundary condition conveniently treats all diffraction patterns and object pixels in the same way by assuming that $\mathbb{Z}_n^2$ is a (discrete) torus. The periodic boundary condition generally forces the slope $\mathbf{r}$ in the linear phase ambiguity to be integers. The dark-field and bright-field boundary conditions assume zero and nonzero values, respectively, in $\mathcal{M} \setminus \mathbb{Z}_n^2$.

Depending on our knowledge of the boundary values, we may or may not enforce the boundary condition in each case. When the bright-field boundary condition is enforced, the linear phase ambiguity disappears from the object estimate. On the contrary, enforcing the dark-field boundary condition can not remove the linear phase ambiguity. In both cases, however, enforcing either boundary condition speeds up the convergence as shown in Figure 7 which is produced by keeping the maximum iterations of the inner loops to 30.

Moreover, the dark-field boundary condition can pose a challenge for reconstruction if the object domain has many dark pixels as in the case of RPP. Fig. 8(a) shows an example of failed reconstruction with PPC(0,0,0.5) of RPP which has a piece of the shell shifted sideway. There are several ways to fix the problem: One is to improve the initialization condition, another is to use a different boundary conditions (periodic or bright-field BC) and yet another is to increase the number of iterations in the inner loops. Fig. 8(b) shows the reconstructed phase error with the periodic BC (note the scale of the color bar). Fig. 7(b) shows the relative error with probe initialization PPC(0, 0, 0.4) and various boundary conditions.

3.8. **Linear phase ambiguity.** To show that the linear phase ambiguity is absent under the bright-field boundary condition, we test AMDRS with the initialization PPC$(-0.5, 0.5, \frac{1}{2})$ and use a more stringent error metric

$$\text{RE2}(k) \quad = \quad \min_{\alpha \in \mathbb{C}} \frac{\|f(\mathbf{k}) - \alpha f_k(\mathbf{k})\|_2}{\|f\|_2}. \tag{24}$$

Note that PPC$(-0.5, 0.5, \frac{1}{2})$ violates the probe phase constraint $\Re(\bar{\nu}^0 \odot \mu^0) > 0$ allowed by the uniqueness theory. The linear phase factor is introduced in the initialization to test if it persists in the reconstruction.

We also use the less tolerant stopping rule

$$\frac{\||A_k A_k^\dagger u_k^l| - b\|_2 - \||A_k A_k^\dagger u_k^{l+1}| - b\|_2}{\||A_k A_k^\dagger u_k^l| - b\|_2} \leq 10^{-5}$$

for the inner loops with the maximum number of iteration capped at 80, the rate of convergence accelerates.

Fig. 9 demonstrates the capability of the bright-field boundary condition to eliminate the linear phase ambiguity as the stronger error metric (24) decays geometrically before settling down to the final level of accuracy. The higher boundary value (255 in Fig. 9(a)) leads to faster convergence than the lower boundary value (100 in Fig. 9(b)). The final level of accuracy, however, depends on how accurately the inner loops for each epoch are solved. For example, increasing the maximum number of iteration from 80 to 110, significantly enhances the final accuracy of reconstruction (not shown).

4. Conclusion

We have presented reconstruction algorithms based on alternating minimization by Douglas-Rachford splitting. Our choices of the objective functions and the step size are informed by the uniqueness theory [13], the Poisson noise model and the stability analysis. The confluence of the three considerations leads to the proposed scheme AMDRS.

Enabled by the PPC initialization method, AMDRS converges globally and geometrically in all our experiments except in the case of RPP with the dark-field boundary condition and the initialization condition PPC(0, 0, 0.5) due to the extensive area of dark pixels.

The boundary condition can have a significant impact on the performance of numerical reconstruction. For either the dark-field or bright-field condition, enforcing the boundary condition, whenever available, improves the rate of convergence.

Appendix A. The Poisson versus Gaussian log-likelihood functions

Poisson distribution

$$P(n) = \frac{\lambda^n e^{-\lambda}}{n!}$$

Let $n = \lambda(1+\epsilon)$ where $\lambda \gg 1$ and $\epsilon \ll 1$. Using Stirling's formula

$$n! \sim \sqrt{2\pi n} e^{-n} n^n$$

in the Poisson distribution, we obtain

$$\begin{aligned} P(n) &\sim \frac{\lambda^{\lambda(1+\epsilon)} e^{-\lambda}}{\sqrt{2\pi} e^{-\lambda(1+\epsilon)} [\lambda(1+\epsilon)]^{\lambda(1+\epsilon)+1/2}} \\ &\sim \frac{1}{\sqrt{2\pi\lambda} e^{-\lambda\epsilon} (1+\epsilon)^{\lambda(1+\epsilon)+1/2}}. \end{aligned}$$

By the asymptotic

$$(1+\epsilon)^{\lambda(1+\epsilon)+1/2} \sim e^{\lambda\epsilon+\lambda\epsilon^2/2}$$

we have

$$P(n) \sim \frac{e^{-\lambda\epsilon^2/2}}{\sqrt{2\pi\lambda}} = \frac{e^{-(n-\lambda)^2/(2\lambda)}}{\sqrt{2\pi\lambda}}. \tag{25}$$

Namely in the low noise limit the Poisson noise is equivalent to the Gaussian noise of the mean $|y_0|^2$ and the variance equal to the intensity of the diffraction pattern. The overall SNR can be tuned by varying the signal energy $\|y_0\|^2$.

The log-likelihood function for the right hand side of (25) is

$$\sum_j \ln|y[j]| + \frac{1}{2}\left|\frac{b[j]}{|y[j]|} - |y[j]|\right|^2, \quad b = \text{noisy diffraction pattern}. \tag{26}$$

For small NSR and in the vicinity of b, we make the substitution

$$\frac{\sqrt{b[j]}}{|y[j]|} \to 1, \quad \ln|y[j]| \to \ln\sqrt{b[j]}$$

to obtain

$$\text{const.} + \frac{1}{2}\sum_j \left|\sqrt{b[j]} - |y[j]|\right|^2. \tag{27}$$

Appendix B. Proof of Proposition 2.1

Note that $A_\infty^\dagger u = A_\infty^\dagger x, B_\infty^\dagger v = B_\infty^\dagger y$ and

$$\begin{aligned} P_\infty u &= P_\infty x, \qquad P_\infty^\perp u = -P_\infty^\perp x \\ Q_\infty v &= Q_\infty y, \qquad Q_\infty^\perp v = -Q_\infty^\perp y, \end{aligned}$$

Hence we also have $u = R_\infty x, \quad v = S_\infty y$.

There are two ways to express (18)-(19) in terms of y, x: First, by reorganizing,

$$b \odot \mathrm{sgn}(x) = P_\infty x - \rho P_\infty^\perp x \tag{28}$$

$$b \odot \mathrm{sgn}(y) = Q_\infty y - \rho Q_\infty^\perp y, \tag{29}$$

and, second, after the reflections R_∞ and S_∞, respectively,

$$P_\infty x + \rho P_\infty^\perp x = R_\infty\left(b \odot \mathrm{sgn}(x)\right) \tag{30}$$

$$Q_\infty y + \rho Q_\infty^\perp y = S_\infty\left(b \odot \mathrm{sgn}(y)\right). \tag{31}$$

From (28)-(29) we obtain by the Pythogoras theorem

$$\|P_\infty x\|_2^2 + \rho^2\|P_\infty^\perp x\|_2^2 = \|b\|_2^2 = \|Q_\infty y\|_2^2 + \rho^2\|Q_\infty^\perp y\|_2^2. \tag{32}$$

If $\|P_\infty^\perp x\|_2 = 0$, then $x = P_\infty x = b \odot \mathrm{sgn}(x)$ by (28), implying $b = |A_\infty f_\infty|$ for $f_\infty := A_\infty^\dagger u = A^\dagger x$. Likewise, if $\|Q_\infty^\perp y\|_2 = 0$, then $y = Q_\infty y = b \odot \mathrm{sgn}(y)$ by (29), implying $b = |B_\infty \mu_\infty|$ for $\mu_\infty := B_\infty^\dagger v = B_\infty^\dagger y$. In other words, (f_∞, μ_∞) solve the blind ptychography problem.

We now prove Proposition 2.1 by contradiction. For our purpose, it suffices to focus on (28).

Suppose $\|P_\infty x\|_2 < \|b\|_2$ (or equivalently $\|P_\infty^\perp x\|_2 \neq 0$). Applying Ω^* and rewriting (30) we have

$$CC^\dagger|x| + \rho(|x| - CC^\dagger|x|) \;=\; 2CC^\dagger b - b \tag{33}$$

On the other hand, applying the operator $C^\dagger$ on (33) we have

$$C^\dagger|x| = C^\dagger b.$$

Combining the above two relations, we obtain

$$CC^\dagger|x| = CC^\dagger b = \frac{\rho|x|}{1+\rho} + \frac{b}{1+\rho}. \tag{34}$$

Using (34) we now show that $\|J_A(\eta)\| > \|\eta\|$ if $\rho \geq 1$ and $\eta = \imath(\alpha|x| + \beta b)$ where α and β are two positive constants such that $\rho\beta > \alpha$. The choice of a purely imaginary η is to nullify $\Re\big(\eta - 2CC^\dagger\eta\big)$ by means of (34). By (34), η can be written as

$$\eta \;=\; \imath(\alpha + \frac{\alpha}{\rho})CC^\dagger|x| + \imath(\beta - \frac{\alpha}{\rho})b$$

After some algebra with (20) and (34), we arrive at

$$J_A(\eta) = \frac{\imath}{1+\rho}\left\{\left[\frac{\rho(\rho-1)}{\rho+1}(\alpha+\beta)+\alpha\right]|x| + 2\left[\frac{2\beta\rho}{\rho+1} + \frac{\alpha(\rho-1)}{\rho+1}\right]b + \left[\frac{2\alpha}{\rho+1} + \frac{(1-\rho)\beta}{1+\rho}\right]\frac{b^2}{|x|}\right\}$$

For the rest of our analysis the case of $\rho = 1$ is particularly transparent.

For $\rho = 1$,

$$J_A(\eta) = \frac{\imath}{2}\left[\alpha|x| + 2\beta b + \alpha b^2/|x|\right].$$

By the quadratic inequality, $\alpha|x| + \alpha b^2/|x| \geq 2\alpha b$ and hence $\|J_A(\eta)\|_2 \geq (\alpha+\beta)\|b\|_2$. On the other hand, by (38), $\eta = \imath 2\alpha CC^\dagger|x| + \imath(\beta-\alpha)b$ and hence

$$\|\eta\|_2 \;\leq\; 2\alpha\|CC^\dagger x\|_2 + (\beta-\alpha)\|b\|_2$$

where $\alpha < \beta$. Therefore, as a consequence of $\||CC^\dagger|x|\|_2 = \|P_\infty x\|_2 < \|b\|_2$, the desired result follows:

$$\|\eta\|_2 < (\alpha+\beta)\|b\|_2 \leq \|J_A(\eta)\|_2.$$

Finally, for any linearly stable fixed point of Gaussian DRS, we now know from the above analysis that $\|P_\infty^\perp x\|_2 = 0$ and hence $x = P_\infty x$ which, combined with (28), yields the sought after statement (21).

Appendix C. Proof of Proposition 2.2

As we have seen in the proof of Proposition 2.1 that any blind ptychography solution satisfies $x = P_\infty x = b \odot \mathrm{sgn}(x)$ and hence by (20)

$$\begin{aligned} J_A(\eta) &= CC^\dagger\eta + \frac{1}{1+\rho}\Re\big(\eta - 2CC^\dagger\eta\big) \\ &= \imath\Im\left(CC^\dagger\eta\right) + \Re\left(CC^\dagger\eta\right) + \frac{1}{1+\rho}\Re\big(\eta - 2CC^\dagger\eta\big). \end{aligned} \tag{35}$$

We now show that $\|J_A(\eta)\|_2 \le \|\eta\|_2$ for all η. The case for J_B can be similarly analyzed.

To proceed, we shall write $CC^\dagger = GG^*$ where G is an isometry. This can be done for any matrix C via the QR decomposition.

According to Proposition 5.9 and Corollary 5.10 in [5], GG^* can be block-diagonalized into one $(N-2n^2)\times(N-2n^2)$ zero block and $2n^2$ 2×2 blocks

$$\begin{bmatrix} \lambda_k^2 & \lambda_k\lambda_{2n^2+1-k} \\ \lambda_k\lambda_{2n^2+1-k} & \lambda_{2n^2+1-k}^2 \end{bmatrix}, \quad k = 1, 2, \cdots, 2n^2 \tag{36}$$

in the orthonormal basis $\{\eta_k, \imath\eta_{2n^2+1-k} : k = 1, 2, \cdots, 2n^2\}$ where $\eta_k \in \mathbb{R}^N$ are the right singular vectors, corresponding to the singular values λ_k, of

$$\begin{bmatrix} \Re[K^*] \\ \Im[K^*] \end{bmatrix} \in \mathbb{R}^{2n^2, N}. \tag{37}$$

Moreover, the complete set of singular values satisfy

$$1 = \lambda_1 \ge \lambda_2 \ge \cdots \ge \lambda_{2n^2} = \lambda_{2n^2+1} = \cdots = \lambda_N = 0 \tag{38}$$

$$\lambda_k^2 + \lambda_{2n^2+1-k}^2 = 1. \tag{39}$$

In view of the block-diagonal nature of GG^*, we shall analyze $J_A(\eta)$ in the 2-dim spaces spanned by the orthonormal basis $\{\eta_k, \imath\eta_{2n^2+1-k}\}$ one k at a time. Note that the first basis vector η_k is real and the second $\imath\eta_{2n^2+1-k}$ is purely imaginary.

For any fixed k, we write $\eta = (z_1, z_2)^T \in \mathbb{C}^2$ and obtain

$$\begin{aligned} J_A(\eta) &= \left(\lambda_k^2 z_1 + \lambda_k\lambda_{2n^2+1-k} z_2\right)\eta_k + \left(\lambda_k\lambda_{2n^2+1-k} z_1 + \lambda_{2n^2+1-k}^2 z_2\right)\imath\eta_{2n^2+1-k} \\ &\quad + \frac{1}{1+\rho}\left[(1-2\lambda_k^2)\Re(z_1) - 2\lambda_k\lambda_{2n^2+1-k}\Re(z_2)\right]\eta_k \\ &\quad + \frac{1}{1+\rho}\left[2\lambda_k\lambda_{2n^2+1-k}\Im(z_1) - (1-2\lambda_{2n^2+1-k}^2)\Im(z_2)\right]\eta_{2n^2+1-k}. \end{aligned} \tag{40}$$

Next we treat (40) as a linear function of $\Re(z_1), \Re(z_2), \Im(z_1), \Im(z_2)$ with real coefficients in the basis $\{\eta_k, \imath\eta_{2n^2+1-k}, \imath\eta_k, \eta_{2n^2+1-k}\}$ and represent J_A by a 4×4 matrix which is block-diagonalized into two 2×2 blocks:

$$\begin{bmatrix} \frac{1}{1+\rho} + \frac{\rho-1}{\rho+1}\lambda_k^2 & \frac{\rho-1}{\rho+1}\lambda_k\lambda_{2n^2+1-k} \\ \lambda_k\lambda_{2n^2+1-k} & \lambda_{2n^2+1-k}^2 \end{bmatrix}, \quad \begin{bmatrix} \lambda_k^2 & \lambda_k\lambda_{2n^2+1-k} \\ -\frac{\rho-1}{\rho+1}\lambda_k\lambda_{2n^2+1-k} & -\frac{1}{\rho+1} - \frac{\rho-1}{\rho+1}\lambda_{2n^2+1-k}^2 \end{bmatrix}. \tag{41}$$

with the former of (41) acting on $\Re(z_1), \Re(z_2)$ and the latter acting on $\Im(z_1), \Im(z_2)$. In view of their similar structure, it suffices to focus on the former.

Calculation of the eigenvalues with (38)-(39) gives

$$\frac{1}{2(\rho+1)}\left[\rho+2(1-\lambda_k^2)\pm\sqrt{\rho^2-4\lambda_k^2+4\lambda_k^4}\right] \tag{42}$$

which, with the + sign, equals 1 at $k=2n^2$ (recall $\lambda_{2n^2}=0$). Next we show that 1 is the largest eigenvalue among all k and $\rho\in[0,\infty)$.

Note that the radical in (42) is real for any $\lambda_k\in[0,1]$ iff $\rho\geq 1$. Hence, for $\rho\geq 1$, the maximum eigenvalue is 1 and occurs at $k=2n^2$. In particular, (42) becomes

$$\frac{1}{4}\left[1+2(1-\lambda_k^2)\pm|1-2\lambda_k^2|\right] \quad \text{for} \quad \rho=1, \tag{43}$$

which achieves the maximum value 1 at $k=2n^2$ and the second largest eigenvalue $1-\lambda_{2n^2-1}^2$ at $k=2n^2-1$.

For $\rho<1$ and those k's giving rise to some purely imaginary radical in (42), we calculate the modulus of (42) and obtain the upper bound

$$\sqrt{\frac{1-\lambda_k^2}{1+\rho}}\leq\sqrt{\frac{1}{1+\rho}}\leq 1, \quad \forall k. \tag{44}$$

In view of (42) and the leftmost term in (44), it is clear that the second largest (in modulus) eigenvalue also occurs at $k=2n^2-1$.

According Proposition 5.6 in [5], $\eta_1=b$ and hence $\arg\min_{\|\eta\|=1}|J_A(\eta)|$ occurs in the subspace spanned by $\{\eta_{2n^2},\imath b\}$ where η_{2n^2} is a real-valued null vector of (37). It is easy to check that a real null vector of (37) is also a null vector of K^* and hence of P_∞. Since x is in the range of P_∞, we conclude that $\arg\min_{\|\eta\|=1}|J_A(\eta)|$ contains $\pm\imath b/\|b\|$ and possibly elsewhere since we do not know if $\lambda_k>0$ for $k>2n^2$ without additional conditions.

The proof is complete.

Appendix D. Initialization by feature extraction

Initialization plays an important role in any non-convex iterative method. In [7], we develop a theory of initialization for phase retrieval based on *feature extraction*.

With a known probe, we cast the problem in the form $b=|Af|$. We consider the simple feature corresponding to "weak signals" in each diffraction patterns, defined by intensities less than certain threshold. Specifically, for each diffraction pattern k, the weak signals are those less than some chosen threshold τ_k and we collect the corresponding indices in the set I_k. Let $I=\cup_k I_k$. We then initialize the object estimate by the feature given by the *ground state* of the sub-row matrix A_I. We call the resulting initialization the null vector denoted by f_{null}, i.e.

$$f_{\text{null}} \;=\; \arg\min\left\{\|A_I x\|^2 : \|x\|=1\right\} \tag{45}$$

which can be solved simply.

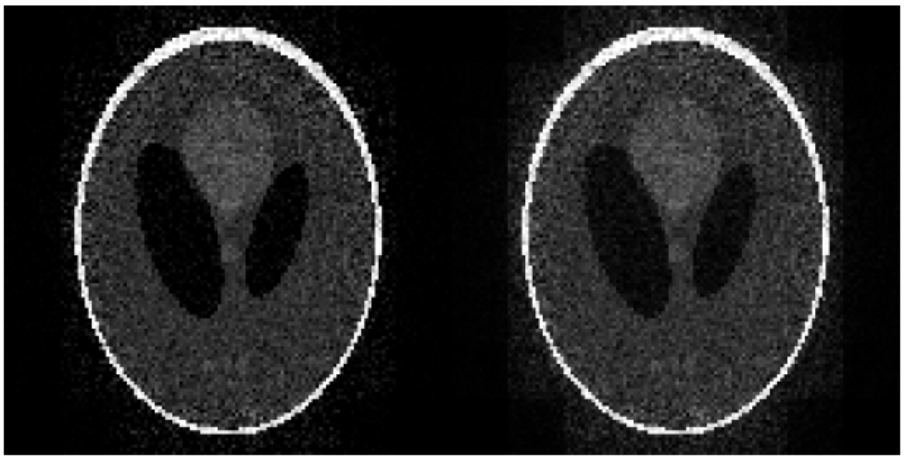

FIGURE 10. Null initialization with the regular raster scan for RPP showing $|\mathrm{sgn}(f^*) \odot f_{\mathrm{null}}|$ (left) and $|f_{\mathrm{null}}|$ (right).

A simple choice of τ_k is that exactly *half* of the signals in each diffraction pattern are weak, i.e. $|I_k| = 2m^2$ and τ_k is the median value of the diffraction pattern k. Fig. 10 shows the results of the null initialization with such a threshold and 50% overlap between adjacent probes in the regular raster scan. Evident from Fig.10, the null initialization captures well the primary feature of the object.

ACKNOWLEDGEMENTS

The research of A. F. is supported by the US National Science Foundation grant DMS-1413373. AF thanks National Center for Theoretical Sciences (NCTS), Taiwan, where the present work was carried out, for the hospitality during his visits in June and August 2018.

REFERENCES

[1] B. Abbey, K. A. Nugent, G. J. Williams, J.N. Clark, A.G. Peele , M.A. Pfeiffer, M. De Jonge & I. McNulty, "Keyhole coherent diffractive imaging." *Nat. Phys.* **4** (2008) 394-398.

[2] L. Bian, J. Suo, J. Chung, X. Ou, C. Yang, F. Chen, and Q. Dai, "Fourier ptychographic reconstruction using Poisson maximum likelihood and truncated Wirtinger gradient," *Sci. Rep.* **6** (2016), 27384.

[3] O. Bunk, M. Dierolf, S. Kynde, I. Johnson, O. Marti, F. Pfeiffer, "Influence of the overlap parameter on the convergence of the ptychographical iterative engine," *Ultramicroscopy* **108** (5) (2008) 481-487.

[4] H.N. Chapman & K.A. Nugent, "Coherent lensless X-ray imaging," *Nat. Photon.* **4** (2010) 833-839.

[5] P. Chen and A. Fannjiang, "Phase retrieval with a single mask by Douglas-Rachford algorithms," *Appl. Comput. Harmon. Anal.* **44** (2018), 665-699.

[6] P. Chen and A. Fannjiang, " Coded-aperture ptychography: uniqueness and reconstruction", *Inverse Problems* **34** (2018) 025003.

[7] P. Chen, A. Fannjiang and G. Liu, "Phase retrieval by linear algebra," *SIAM J. Matrix Anal. Appl.* **38** (2017) 854-868.

[8] P. Chen, A. Fannjiang and G. Liu, "Phase retrieval with one or two coded diffraction patterns by alternating projection with the null initialization," *J. Fourier Anal. Appl.* **24** (2018), 719-758.

[9] M. Dierolf, A. Menzel, P. Thibault, P. Schneider, C. M. Kewish, R. Wepf, O. Bunk, and F. Pfeiffer, " Ptychographic x-ray computed tomography at the nanoscale," *Nature* **467** (2010), 436-439.
[10] J. Douglas and H.H. Rachford, "On the numerical solution of heat conduction problems in two and three space variables," *Trans. Am. Math. Soc.***82** (1956), 421-439.
[11] V. Elser, "Phase retrieval by iterated projections," *J. Opt. Soc. Am. A* **20** (2003), 40-55.
[12] J. Eckstein and D.P. Bertsekas, "On the Douglas-Rachford splitting method and the proximal point algorithm for maximal monotone operators," *Math. Program. A* **55** (1992), 293-318.
[13] A. Fannjiang & P. Chen, "Blind ptychography: uniqueness and ambiguities," `arXiv:1806.02674`.
[14] A. Fannjiang and W. Liao, "Fourier phasing with phase-uncertain mask," *Inverse Problems* **29** (2013) 125001.
[15] H.M.L. Faulkner and J.M. Rodenburg, "Movable aperture lensless transmission microscopy: A novel phase retrieval algorithm," *Phys. Rev. Lett.***93** (2004), 023903.
[16] H.M.L. Faulkner and J.M. Rodenburg, "Error tolerance of an iterative phase retrieval algorithm for moveable illumination microscopy," *Ultramicroscopy* **103:2** (2005), 153-164.
[17] D. Gabay and B. Mercier. A dual algorithm for the solution of nonlinear variational problems via finite element approximation. *Computers & Mathematics with Applications* **2(1)** (1976), 17-40.
[18] S. Gao, P. Wang, F. Zhang, G. T. Martinez, P. D. Nellist, X. Pan & A. I. Kirkland, "Electron ptychographic microscopy for three-dimensional imaging," *Nat. Comm.* **18**(2017) 163.
[19] R. Glowinski and A. Marroco. "Sur l'approximation, par éléments finis d'ordre un, et la résolution, par pénalisation-dualité d'une classe de problémes de dirichlet non linéaires," *ESAIM: Mathematical Modelling and Numerical Analysis*, **9**(1975), 41-76.
[20] P. Godard, M. Allain, V. Chamard, and J. Rodenburg, "Noise models for low counting rate coherent diffraction imaging," *Opt. Express* **20** (2012), 25914-25934.
[21] M. Guizar-Sicairos, J.R. & Fienup, "Phase retrieval with transverse translation diversity: a nonlinear optimization approach." *Opt. Express* **16** (2008), 7264-7278.
[22] R. Hesse, D. R. Luke, S. Sabach, and M.K. Tam, "Proximal heterogeneous block implicit-explicit method and application to blind ptychographic diffraction imaging," *SIAM J. Imag. Sci.* **8** (2015) pp. 426-457.
[23] R. Horisaki, R. Egami & J. Tanida, "Single-shot phase imaging with randomized light (SPIRaL)". *Opt. Express* **24** (2016), 3765-3773.
[24] X. Huang, H. Yang, R. Harder, Y. Hwu, I.K. Robinson & Y.S. Chu,"Optimization of overlap uniformness for ptychography," *Opt. Express* **22** (2014), 12634-12644.
[25] Y. Jiang, Z. Chen, Y. Han, P. Deb, H. Gao, S. Xie, P. Purohit, M. W. Tate, J. Park, S. M. Gruner, V. Elser & D. A. Muller "Electron ptychography of 2D materials to deep sub-angstrom resolution," *Nature* **559** (2018) 343-349.
[26] C. Kohler, F. Zhang and W. Osten, "Characterization of a spatial light modulator and its application in phase retrieval," *Appl. Opt.* **48** (2009) 4003-4008.
[27] A.P. Konijnenberg, W.M.J. Coene and H.P. Urbach, "Model-independent noise-robust extension of ptychography," *Opt. Exp.***26** (2018) 5857-5874.
[28] C. Kuang, Y. Ma, R. Zhou, J. Lee, G. Barbastathis, R. R. Dasari, Z. Yaqoob & P.T.C. So, "Digital micromirror device-based laser-illumination Fourier ptychographic microscopy," *Opt. Exp.* **23**(2015), 26999-27010.
[29] G. Li & T. K. Pong, "DouglasRachford splitting for nonconvex optimization with application to nonconvex feasibility problems," *Math. Program.* **A 159** (2016), 371-401
[30] P.-L. Lions and B. Mercier,"Splitting algorithms for the sum of two nonlinear operators," *SIAM J. Num. Anal.* **16** (1979), 964-979.
[31] A. M. Maiden, M. J. Humphry, F. Zhang and J. M. Rodenburg, "Superresolution imaging via ptychography," *J. Opt. Soc. Am. A* **28** (2011), 604-612.
[32] A. M. Maiden, D. Johnson and P. Li, "Further improvements to the ptychographical iterative engine," *Optica* **4** (2017), 736-745.
[33] A.M. Maiden, G.R. Morrison, B. Kaulich, A. Gianoncelli & J.M. Rodenburg, "Soft X-ray spectromicroscopy using ptychography with randomly phased illumination," *Nat. Commun.* **4** (2013), 1669.

[34] A.M. Maiden & J.M. Rodenburg, "An improved ptychographical phase retrieval algorithm for diffractive imaging," *Ultramicroscopy* **109** (2009), 1256-1262.
[35] A. M. Maiden, J. M. Rodenburg and M. J. Humphry, "Optical ptychography: a practical implementation with useful resolution," *Opt. Lett.* **35** (2010), 2585-2587.
[36] G.R. Morrison, F. Zhang, A. Gianoncelli and I.K. Robinson, "X-ray ptychography using randomized zone plates," *Opt. Exp.* **26** (2018) 14915-14927.
[37] Y. S. G. Nashed, D. J. Vine, T. Peterka, J. Deng, R. Ross and C. Jacobsen, "Parallel ptychographic reconstruction," *Opt. Express* **22** (2014) 32082-32097.
[38] P.D. Nellist, B.C. McCallum & J.M. Rodenburg, "Resolution beyond the information limit in transmission electron microscopy, " *Nature* **374** (1995) 630-632.
[39] P.D. Nellist and J.M. Rodenburg, " Electron ptychography. I. Experimental demonstration beyond the conventional resolution limits," *Acta Cryst. A* **54** (1998), 49-60.
[40] K.A. Nugent, "Coherent methods in the X-ray sciences, " *Adv. Phys.***59** (2010) 1-99.
[41] X. Ou, G. Zheng and C. Yang, "Embedded pupil function recovery for Fourier ptychographic microscopy," *Opt. Exp.* **22** (2014) 4960-4972.
[42] X. Peng, G.J. Ruane, M.B. Quadrelli & G.A. Swartzlander, " Randomized apertures: high resolution imaging in far field," *Opt. Express* **25** (2017) 296187.
[43] F. Pfeiffer, "X-ray ptychography," *Nat. Photon.* **12** (2017) 9-17.
[44] J.M. Rodenburg, "Ptychography and related diffractive imaging methods," *Adv. Imaging Electron Phys.* **150** (2008) 87-184.
[45] J.M. Rodenburg and H.M.L. Faulkner, "A phase retrieval algorithm for shifting illumination". *Appl. Phys. Lett.* **85** (2004), 4795.
[46] M.H. Seaberg, A. d'Aspremont & J.J. Turner, "Coherent diffractive imaging using randomly coded masks," *Appl. Phys. Lett.* **107** (2015) 231103.
[47] P. Sidorenko, O. Lahav, Z. Avnat & O. Cohen, "Ptychographic reconstruction algorithm for frequency-resolved optical gating: super-resolution and supreme robustness," *Optica* **3** (2016) 1320-1330.
[48] J.C. Silva and A. Menzel, "Elementary signals in ptychography," *Opt. Exp.* **23** (2015) 33812-33821.
[49] M. Stockmar, P. Cloetens, I. Zanette, B. Enders, M. Dierolf, F. Pfeiffer, and P. Thibault,"Near-field ptychography: phase retrieval for inline holography using a structured illumination," *Sci. Rep.* **3** (2013), 1927.
[50] D. Sylman, V. Micó, J. Garca & Z. Zalevsky, "Random angular coding for superresolved imaging," *Appl. Opt.***49** (2010), 4874-4882.
[51] P. Thibault, M. Dierolf, O. Bunk, A. Menzel, F. Pfeiffer, "Probe retrieval in ptychographic coherent diffractive imaging," *Ultramicroscopy* **109** (2009), 338-343.
[52] P. Thibault, M. Dierolf, A. Menzel, O. Bunk, C. David, F. Pfeiffer, "High-resolution scanning X-ray diffraction microscopy", *Science* **321** (2008), 379-382.
[53] P. Thibault and M. Guizar-Sicairos, " Maximum-likelihood refinement for coherent diffractive imaging". *New J. Phys.* **14** (2012), 063004.
[54] L. Tian, Z. Liu, L-H Yeh, M. Chen, J. Zhong, L. Waller, "Computational illumination for high-speed in vitro Fourier ptychographic microscopy," *Optica* **2** (2015) 904-911.
[55] L. Valzania, T. Feurer, P. Zolliker & E. Hack, "Terahertz ptychography," *Opt. Lett.* **43** (2018), 543-546.
[56] Z. Wen, C. Yang, X. Liu and S. Marchesini, "Alternating direction methods for classical and ptychographic phase retrieval," *Inverse Problems* **28** (2012), 115010.
[57] L. Yeh, J. Dong, J. Zhong, L.Tian, M. Chen, G. Tang, M. Soltanolkotabi, and L. Waller, "Experimental robustness of Fourier ptychography phase retrieval algorithms," *Optics Express* **23** (2015) 33214-33240.
[58] F. Zhang, B. Chen, G. R. Morrison, J. Vila-Comamala, M. Guizar-Sicairos & I. K. Robinson, "Phase retrieval by coherent modulation imaging," *Nat. Comm.* **7** (2016):13367.
[59] F. Zhang, G. Pedrini & W. Osten, "Phase retrieval of arbitrary complex-valued fields through aperture-plane modulation," *Phys. Rev. A* **75** (2007), 043805.

[60] Y. Zhang, P. Song, Q. Dai, "Fourier ptychographic microscopy using a generalized Anscombe transform approximation of the mixed Poisson-Gaussian likelihood," *Opt. Exp.* **25** (2017) 168-179.
[61] G. Zheng, R. Horstmeyer and C.Yang, "Wide-field, high-resolution Fourier ptychographic microscopy," *Nature Photonics* **7** (2013), 739-745.
[62] C. Zuo, J. Sun and Q. Chen, "Adaptive step-size strategy for noise-robust Fourier ptychographic microscopy," *Optics Express* **24** (2016), 20724-20744.

DEPARTMENT OF MATHEMATICS, UNIVERSITY OF CALIFORNIA, DAVIS, CALIFORNIA 95616, USA. EMAIL: FANNJIANG@MATH.UCDAVIS.EDU

DEPARTMENT OF MATHEMATICS, UNIVERSITY OF CALIFORNIA, DAVIS, CALIFORNIA 95616, USA.